

# **Determination of the beam asymmetry $\Sigma$ in $\eta$ - and $\eta'$ -photoproduction using Bayesian statistics**

JAKOB MICHAEL KRAUSE

Masterarbeit in Physik  
angefertigt im Helmholtz-Institut für Strahlen- und  
Kernphysik

vorgelegt der  
Mathematisch-Naturwissenschaftlichen Fakultät  
der  
Rheinischen Friedrich-Wilhelms-Universität  
Bonn

Sep 2022

DRAFT

I hereby declare that this thesis was formulated by myself and that no sources or tools other than those cited were used.

Bonn, .....  
Date

.....  
Signature

- 1. Gutachterin: JUN. PROF. DR. ANNIKA THIEL
- 2. Gutachter: PROF. DR. JOCHEN DINGFELDER

DRAFT

# Contents

---

<b>1</b>	<b>Introduction</b>	<b>1</b>
1.1	Photoproduction of Pseudoscalar Mesons . . . . .	4
1.2	Measurement of Polarization Observables . . . . .	5
1.3	Introduction to BAYESIAN statistics . . . . .	5
1.3.1	Frequentist Approach . . . . .	5
1.3.2	Bayesian approach . . . . .	5
1.3.3	Combining inferences . . . . .	5
1.4	Motivation and Structure of this Thesis . . . . .	5
<b>2</b>	<b>Experimental Setup</b>	<b>7</b>
2.1	Production of polarized high energy photon beam . . . . .	7
2.1.1	Goniometer . . . . .	11
2.1.2	Tagging system . . . . .	11
2.2	Liquid hydrogen target . . . . .	11
2.3	Calorimeters . . . . .	11
2.4	Trigger . . . . .	11
2.5	Software and Monte Carlo . . . . .	11
2.6	Datasets . . . . .	11
<b>3</b>	<b>Event selection</b>	<b>11</b>
3.1	Reconstruction of events . . . . .	12
3.2	Preselection and charge cut . . . . .	12
3.3	Time of particles . . . . .	13
3.4	Kinematic constraints . . . . .	15
3.4.1	Derivation of cut conditions . . . . .	15
3.4.2	Determination of cut ranges . . . . .	16
3.4.3	Quality of event selection . . . . .	21
3.5	Investigation of background and additional cuts . . . . .	23
3.5.1	Inspecting plausibility of background reactions . . . . .	23
3.5.2	Misidentification of background reactions . . . . .	26
3.5.3	Examination of additional cuts . . . . .	31
3.6	Summary of event selection . . . . .	34
3.6.1	Reaction $\gamma p \rightarrow p\eta' \rightarrow p\gamma\gamma$ . . . . .	34
3.6.2	Reaction $\gamma p \rightarrow p\eta \rightarrow p\gamma\gamma$ . . . . .	35

<b>4</b>	<b>Extraction of the beam asymmetries <math>\Sigma_\eta</math> and <math>\Sigma_{\eta'}</math></b>	<b>37</b>
4.1	Methods . . . . .	38
4.1.1	Event yield asymmetries . . . . .	38
4.1.2	Event based fit . . . . .	41
4.2	Determination of $\Sigma_\eta$ using Bayesian statistics . . . . .	44
4.2.1	Application of methods to toy Monte Carlo data . . . . .	44
4.2.2	Application of methods to data . . . . .	53
4.2.3	Discussion . . . . .	56
4.3	Determination of $\Sigma_{\eta'}$ . . . . .	58
4.3.1	Application of event based fit to toy Monte Carlo data . . . . .	58
4.3.2	Application of event based fit to data . . . . .	64
4.3.3	Systematic error . . . . .	68
<b>5</b>	<b>Discussion</b>	<b>73</b>
5.1	Comparison of results to existing data . . . . .	73
5.2	Comparison of results to PWA calculations . . . . .	75
5.3	Final discussion of methods . . . . .	77
<b>6</b>	<b>Summary and outlook</b>	<b>79</b>
<b>A</b>	<b>Additional plots and calculations</b>	<b>81</b>
A.1	Statistical error for the asymmetry $A(\phi)$ . . . . .	81
A.2	Kinematic variables for each bin . . . . .	83
A.2.1	Coplanarity . . . . .	83
A.2.2	Polar angle difference . . . . .	85
A.2.3	Missing mass . . . . .	87
A.2.4	Invariant mass . . . . .	89
<b>B</b>	<b>Discussion of binned fits</b>	<b>91</b>
<b>C</b>	<b>Investigation of posteriors without truncation</b>	<b>93</b>
	<b>Bibliography</b>	<b>97</b>
	<b>List of Figures</b>	<b>99</b>
	<b>List of Tables</b>	<b>105</b>



## Experimental Setup

In this work the beam asymmetry  $\Sigma$  is determined in the reactions  $\gamma p \rightarrow p\eta$  and  $\gamma p \rightarrow p\eta'$ , requiring a polarized photon beam and an unpolarized proton target. It is convenient to study photoproduction off a fixed target and investigate the resonances that occur in the process. The analyzed data was taken at the CBELSA/TAPS experiment located in Bonn at the ELectron Stretcher Accelerator (ELSA). In this chapter the different parts of the CBELSA/TAPS experiment that are used for the measurement of the beam asymmetry  $\Sigma$  will be presented.

High energy electrons extracted from ELSA are used to produce a polarized photon beam using the *bremsstrahlung* process (see 2.1.1). After they have been energy tagged (see 2.1.2) these photons then interact with the fixed target material (see Section 2.2) so that hadronic resonances may be excited that will decay via the strong interaction under the emission of mesons. The resulting decay products can then be measured with a system of electromagnetic calorimeters and scintillators that is especially suited for the detection of photons (see Section 2.3). The analogue measurements are only saved for offline analysis if detector signals meet certain trigger conditions which is only the case for reactions that are of interest (see Section 2.4). This way the amount of unwanted background is minimized already during the process of data taking. Once data acquisition is finished the data may be investigated with the help of analysis software and Monte Carlo simulations (see Section 2.5) tailored to the needs of the CBELSA/TAPS experiment.

### 2.1 Production of polarized high energy photon beam

To measure polarization observables in photoproduction reactions a polarized photon beam is needed which can be created using *coherent bremsstrahlung*. Bremsstrahlung is the dominating interaction of high energy ( $O(1 \text{ GeV})$ ) electrons with matter [Leo94]. Electrons are decelerated in the COLOUMB field of heavy nuclei and radiate real photons. To conserve momentum there has to be a momentum transfer  $q$  which is negligibly small compared to the nucleon mass. If an amorphous radiator is used incoherent bremsstrahlung is produced with a continuous spectral distribution proportional to  $1/E_\gamma$  according to the BETHE-HEITLER cross section [Hei54]. Since the structure of nuclei in the amorphous radiator does not exhibit any periodicity, the electric field vector will not prefer any particular direction, resulting in a net polarization degree of zero for the photon beam. To achieve non-vanishing polarization degrees a crystal with periodic placement of nuclei may be used as radiator. Then, coherent bremsstrahlung is produced; the crystal can absorb the recoil only for discrete momenta

$q_n$  meeting the LAUE condition of the crystal lattice. This enables constructive interference between different bremsstrahl photons and at the same time fixes the deflection plane of incoming electrons, resulting in a coherent polarized photon beam. Incoherent bremsstrahlung may still occur due to impurities in the crystal structure, so that the total bremsstrahlung cross section off a crystal radiator  $\sigma_{\text{crystal}}$  is the sum of a coherent ( $\sigma_{\text{coherent}}$ ) and an incoherent ( $\sigma_{\text{incoherent}}$ ) part

$$\sigma_{\text{crystal}} = \sigma_{\text{coherent}} + \sigma_{\text{incoherent}}. \quad (2.1)$$

The process of bremsstrahlung can be modeled using ANalytical Bremsstrahlung (ANB) calculations [Nat+03]. ANB intensity spectra for a crystal and amorphous radiator are shown in Figure 2.1 on the left hand side. The right hand side shows the enhancement spectrum, which is given by dividing the two spectra. One observes that the bremsstrahlung intensity spectrum obtained from a crystal radiator

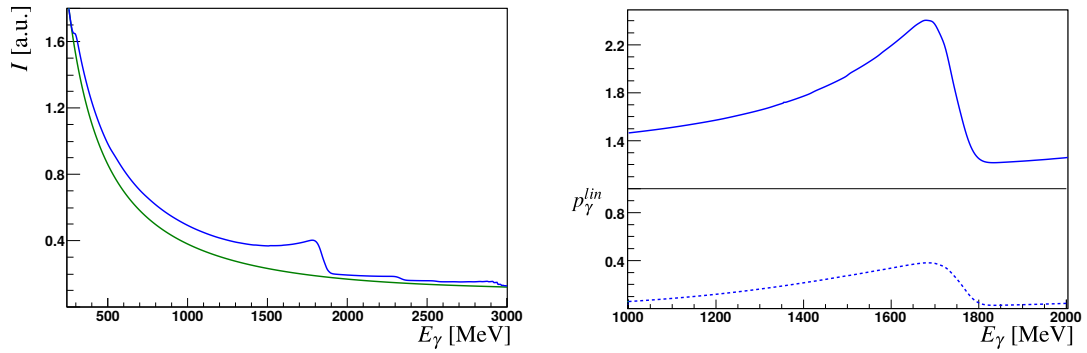


**Figure 2.1:** Left: Incoherent (green) and crystal (blue) bremsstrahlung intensities as a function of the photon energy. Right: The enhancement spectrum is given as the ratio of crystal to incoherent intensity spectrum. The dashed line at the bottom shows the calculated polarization degree. Both spectra are generated using ANB calculations. Taken from [Afz19].

is in general enhanced relative to the incoherent spectrum obtained from an amorphous radiator. In fact, using ANB calculations, the polarization degree can be determined from the enhancement spectrum. The characteristic drop in intensity in the intensity spectrum obtained from the crystal radiator is referred to as the coherent edge. It occurs because the photon energy in the kinematically allowed region of the recoil momentum that will lead to coherent bremsstrahlung is limited. The relative alignment of the radiation crystal to the electron beam determines the position of the coherent edge.

### 2.1.1 Goniometer

To determine the beam polarization, spectra from a diamond radiator as well as from an amorphous radiator are required. Several radiators are placed inside of the goniometer, see Figure ??



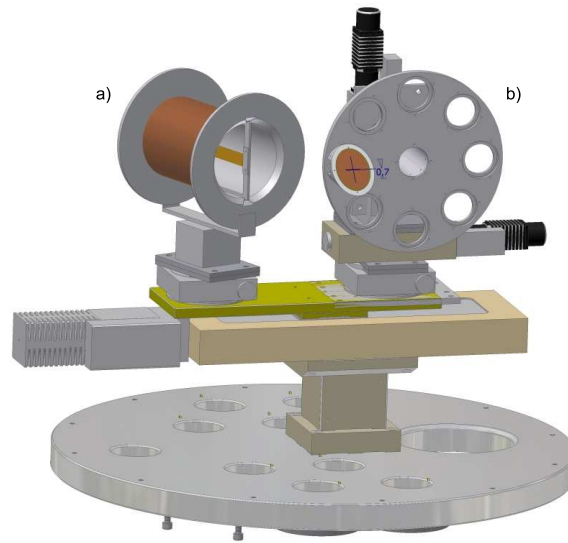


**Figure 2.2:** [Wal]

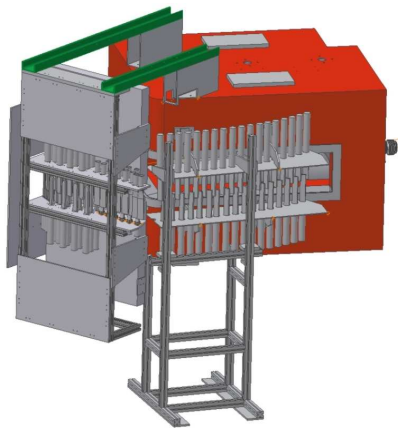


**Figure 2.3:** [Wal]



**Figure 2.4:** [Wal]

### 2.1.2 Tagging system

## 2.2 Liquid hydrogen target

### 2.3 Calorimeters

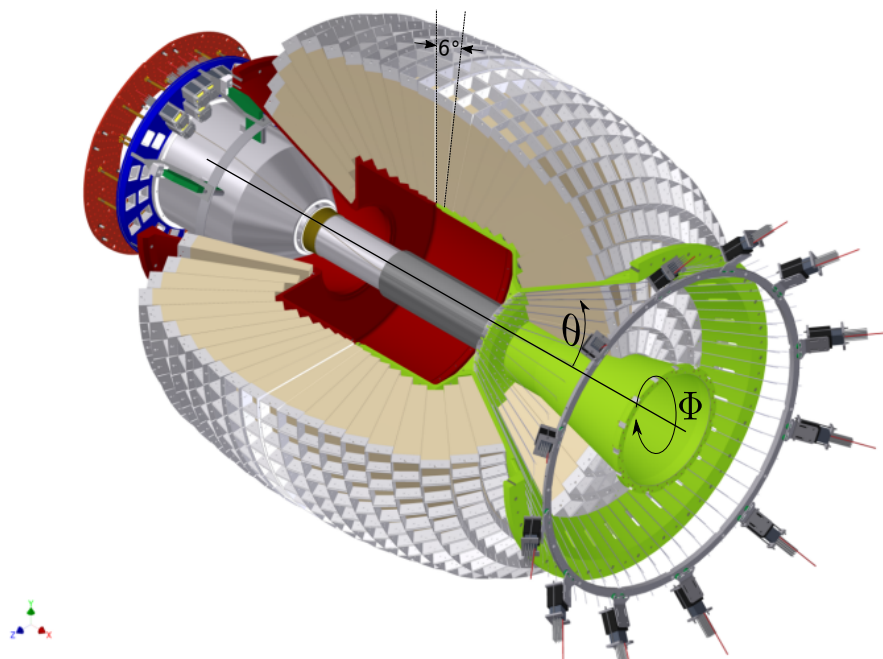


**Figure 2.5:** D. WALTHER in [Urb17]



**Figure 2.6:** [Wal]

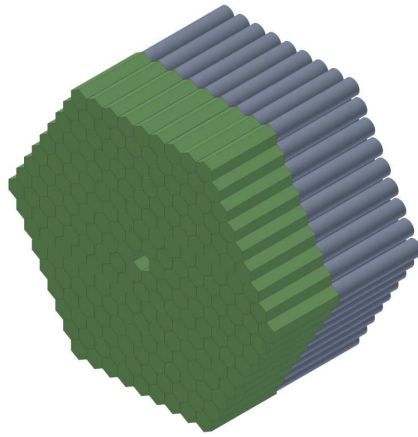


Figure 2.7: [Wal]

## 2.4 Trigger

## 2.5 Software and Monte Carlo

## 2.6 Datasets



# Bibliography

---

- [Leo94] W. R. Leo, *Techniques for Nuclear and Particle Physics Experiments, A How-to Approach*, vol. 2, Springer-Verlag Berlin Heidelberg GmbH, 1994 (cit. on p. 7).
- [Hei54] W. Heithler, *The Quantum Theory of Radiation*, Oxford University Press, 1954 (cit. on p. 7).
- [Nat+03] F. Natter, P. Grabmayr, T. Hehl, R. Owens and S. Wunderlich, *Monte Carlo simulation and analytical calculation of coherent bremsstrahlung and its polarisation*, Nuclear Instruments and Methods in Physics Research Section B: Beam Interactions with Materials and Atoms **211** (2003) 465 (cit. on p. 8).
- [Afz19] F. N. Afzal, *Measurement of the beam and helicity asymmetries in the reactions  $\gamma p \rightarrow p\pi^0$  and  $\gamma p \rightarrow p\eta$* , PhD thesis: Rheinische Friedrich-Wilhelms-Universität Bonn, 2019, URL: <https://hdl.handle.net/20.500.11811/8064> (cit. on p. 8).
- [Wal] D. Walther, *Crystal Barrel, A  $4\pi$  photon spectrometer*, URL: <https://www.cb.uni-bonn.de> (visited on 27/09/2021) (cit. on pp. 9–11).
- [Urb17] M. Urban, *Design eines neuen Lichtpulsersystems sowie Aufbau und Inbetriebnahme der neuen APD Auslese für das Crystal-Barrel-Kalorimeter*, PhD thesis: Rheinische Friedrich-Wilhelms-Universität Bonn, 2017 (cit. on p. 10).



# List of Figures

---

1.1	Running coupling of QCD. The colored data points represent different methods to obtain a value for $\alpha_s$ . For more details it may be referred to [pdg]. . . . .	2
1.2	Calculated nucleon (isospin $I = 1/2$ ) resonances compared to measurements. Left in each column are the calculations [bonnmodel], the middle shows the measurements and PDG rating [pdg] . . . . .	3
1.3	FEYNMAN diagram for the s-channel photoproduction of pseudoscalar mesons, adapted from [Afz19] . . . . .	4
2.1	Left: Incoherent (green) and crystal (blue) bremsstrahlung intensities as a function of the photon energy. Right: The enhancement spectrum is given as the ratio of crystal to incoherent intensity spectrum. The dashed line at the bottom shows the calculated polarization degree. Both spectra are generated using ANB calculations. Taken from [Afz19]. . . . .	8
2.2	[Wal] . . . . .	9
2.3	[Wal] . . . . .	9
2.4	[Wal] . . . . .	9
2.5	D. WALTHER in [Urb17] . . . . .	10
2.6	[Wal] . . . . .	10
2.7	[Wal] . . . . .	11
3.1	Distribution of event classes in $\eta' \rightarrow \gamma\gamma$ production . . . . .	13
3.2	Time information of all final state particles and the beam photon for 3PED $\eta'$ production	14
3.3	Reaction time $t_r$ for 3PED and 2.5PED $\eta'$ production. The yellow region indicate the sidebands while the purple colored interval is the selected prompt peak. . . . .	15
3.4	Coplanarity of the $p\eta'$ final state with all other cuts applied for the energy bin $1500 \text{ MeV} \leq E_\gamma < 1600 \text{ MeV}$ . The vertical dashed lines show the cut ranges obtained from a gaussian fit to the data (open circles). The solid black histograms represent fitted MC data of $\eta' \rightarrow \gamma\gamma$ . . . . .	19
3.5	Polar angle difference of the $p\eta'$ final state with all other cuts applied for the energy bin $1500 \text{ MeV} \leq E_\gamma < 1600 \text{ MeV}$ . The vertical dashed lines show the cut ranges obtained from a gaussian fit to the data (open circles). The solid black histograms represent fitted MC data of $\eta' \rightarrow \gamma\gamma$ . . . . .	20

3.6	Missing mass of the $p\eta'$ final state with all other cuts applied for the energy bin $1500 \text{ MeV} \leq E_\gamma < 1600 \text{ MeV}$ . The vertical dashed lines show the cut ranges obtained from a fit to data (open circles) employing a Novosibirsk function. The solid colored histograms represent fitted MC data from relevant photoproduction reactions: in black $\eta'$ , in green $\pi^0$ , in red $\eta$ , in blue $\omega$ , in yellow $2\pi^0$ , magenta $\pi^0\eta$ . The turquoise histogram is the sum of all MC histograms. . . . .	21
3.7	Invariant mass of the $p\eta'$ final state with all other cuts applied for all energy and angular bins. The open circles represent the measured data, the solid colored histograms fitted MC data from relevant photoproduction reactions: in black $\eta'$ , in green $\pi^0$ , in red $\eta$ , in blue $\omega$ , in yellow $2\pi^0$ and in magenta $\pi^0\eta$ . The turquoise histogram is the sum of all MC histograms. . . . .	22
3.8	Invariant mass of the $p\eta'$ final state with all other cuts applied for the energy bin $1500 \text{ MeV} \leq E_\gamma < 1600 \text{ MeV}$ . The vertical dashed lines show the cut ranges obtained from a gaussian fit to the $\eta'$ MC data (solid black histogram). The open circles represent the measured data, the solid colored histograms fitted MC data from relevant photoproduction reactions: in black $\eta'$ , in green $\pi^0$ , in red $\eta$ , in blue $\omega$ , in yellow $2\pi^0$ and in magenta $\pi^0\eta$ . The turquoise histogram is the sum of all MC histograms. . . . .	22
3.9	Acceptance for the reaction $\gamma p \rightarrow p\eta'$ after all cuts that have been discussed so far for 2.5PED and 3PED events . . . . .	23
3.10	Fraction of background events in the analyzed beam energy and angular bins. . . . .	24
3.11	Acceptance for possible background contributions . . . . .	25
3.12	Generated energies of $\gamma_3$ and $\gamma_4$ in $2\pi^0$ and $\pi^0\eta$ photoproduction MC data. The threshold of 20 MeV is marked by a vertical red line. $E_{\gamma_4}$ is shown on the top, $E_{\gamma_3}$ is shown on the bottom of each figure. . . . .	27
3.13	$E_\gamma^{\text{gen}}$ vs. $E_\gamma^{\text{rec}}$ of $\gamma_1$ and $\gamma_2$ for $2\pi^0$ (top) and $\pi^0\eta$ (bottom) production. The slope $E_\gamma^{\text{gen}} = E_\gamma^{\text{rec}}$ is marked by a solid line. . . . .	29
3.14	Polar angle difference $\Delta\theta$ between $\gamma_2$ and $\gamma_3$ of the $\pi^0\eta$ final state. . . . .	30
3.15	Illustration of the misidentification process during reconstruction. Enumeration of photons is now arbitrary. . . . .	30
3.16	Generated CMS angle $\cos\theta_{\text{gen.}}$ vs. reconstructed CMS angle $\cos\theta_{\text{rec.}}$ for both background reactions. The slope $\cos\theta_{\text{gen.}} = \cos\theta_{\text{rec.}}$ is indicated by the solid line. . . . .	31
3.17	Detector hits of the recoil proton, as obtained from MC data for the production of $\eta'$ , $2\pi^0$ and $\pi^0\eta$ . CB: Crystal Barrel, FW: forward dector, MT: MiniTAPS . . . . .	33
3.18	Difference in measured and calculated beam energy. Data points are shown as open circles, MC data as solid histograms: in black $\eta'$ , in green $\pi^0$ , in red $\eta$ , in blue $\omega$ , in yellow $2\pi^0$ and in magenta $\pi^0\eta$ . The turquoise histogram is the sum of all MC histograms. . . . .	34
3.19	Invariant mass spectrum passing different stages in the event selection process. In the end clear peaks for all possibly produced mesons are visible. The vertical lines indicate the mean cut ranges over all energy and angle bins. . . . .	35
3.20	Invariant mass spectrum passing different stages in the event selection process. In the end clear peaks for all possibly produced mesons are visible. Taken from [Afz19]. . . . .	36



- 
- 4.1 Left: Definition of angles  $\alpha, \phi, \varphi$ . Right: Photon momentum  $\vec{k}$  and polarization  $\vec{\epsilon}$  define the beam polarization plane while the reaction plane is defined by the recoil proton  $p$  and produced meson  $M$ . . . . . 37
- 4.2 Posterior predictive checks  $p(A_{\text{rep}}|A)$  from a BAYESIAN fit to the event yield asymmetries for six toy Monte Carlo bins are shown as distributions. The data points in the upper plot are the asymmetry  $A(\phi)$ , which was additionally fitted using a  $\chi^2$  fit (solid line). The goodness of fit is shown using  $p$ -values, which give the fraction  $T(A_{\text{rep}} > A)$  of replicated samples greater than the original measured value, with propagated statistical error bars on the bottom of each plot. The expected mean value of  $T(A_{\text{rep}} > A) = 0.5$  is indicated by the dashed line. . . . . 46
- 4.3  $p$  values of all toy Monte Carlo bins. They are centered around their mean at 0.5, which is indicated by the dashed line, and show no bias towards higher or lower values, thus confirming an adequate fit. . . . . 47
- 4.4 Left: Combined posterior distributions of all 10000 fits normalized by their respective standard deviation. Right: Unaltered combined posterior distributions of all 10000 fits. A GAUSSIAN fit was performed to determine mean  $\mu$  and standard deviation  $\sigma$  of the distributions with results given on top. . . . . 47
- 4.5 Left: relative error  $\frac{\sigma_{\text{MCSE}}}{\text{median}[p(\Sigma|y)]}$  Right:  $\hat{R}$  associated with the fit parameter  $\Sigma$ . Both are shown for all 10000 fits. The critical values that should not be exceeded are marked by dashed lines. . . . . 48
- 4.6 Combined posteriors for the beam asymmetries  $\Sigma$  and  $\Sigma^{\text{bkg}}$  from all 1000 event based fits. Left: Residuals  $\Xi$  Right: Unnormalized posterior distributions. A GAUSSIAN fit is performed on the distributions with results for mean  $\mu$  and standard deviation  $\sigma$  on top. 50
- 4.7 Combined posterior probabilities using the *pooled likelihood* approach. Left: Signal beam asymmetry, Right: background beam asymmetry. Mean and standard deviation as obtained from a Gaussian fit are shown on top . . . . . 51
- 4.8 Left: relative error  $\frac{\sigma_{\text{MCSE}}}{\text{median}[p(\Sigma|y)]}$  Right:  $\hat{R}$  associated with the fit parameter  $\Sigma$ . Both are shown for all 1000 fits. The critical values that should not be exceeded are marked by dashed lines. . . . . 51
- 4.9 Posterior predictive check using the draws of the detector coefficients  $a$  and  $b$ . Points with error bars are the polarization weighted sum of event yields. The dashed line is the mean of the predictive values while the solid opaque lines are representative of one simulation draw  $a^{(s)}, b^{(s)}$ . . . . . 52
- 4.10 Posterior predictive checks  $p(A_{\text{rep}}|A)$  from a BAYESIAN fit to the event yield asymmetries for all angular bins of the energy bin  $1250 \text{ MeV} \leq E_\gamma < 1310 \text{ MeV}$ . The data points in the upper plot are the asymmetry  $A(\phi)$ , which was additionally fitted using a  $\chi^2$  fit (solid line). The goodness of fit is shown using  $p$ -values, which give the fraction  $T(A_{\text{rep}} > A)$  of replicated samples greater than the original measured value, with propagated statistical error bars on the bottom of each plot. The expected mean value of  $T(A_{\text{rep}} > A) = 0.5$  is indicated by the dashed line. . . . . 54
- 4.11  $p$  values generated using all fits. They are centered around their mean at 0.5, which is indicated by the dashed line, and show no bias towards higher or lower values, thus confirming an adequate fit. . . . . 55

4.12	Left: relative error $\frac{\sigma_{\text{MCSE}}}{\text{median}[p(\Sigma y)]}$ Right: $\widehat{R}$ associated with the fit parameter $\Sigma$ . Both are shown for all $11 \cdot 12$ binned fits to the asymmetry $A(\phi)$ . The critical values that should not be exceeded are marked by dashed lines. . . . .	55
4.13	Left: relative error $\frac{\sigma_{\text{MCSE}}}{\text{median}[p(\Sigma y)]}$ Right: $\widehat{R}$ associated with the fit parameter $\Sigma$ . Both are shown for all $11 \cdot 12$ unbinned fits. The critical values that should not be exceeded are marked by dashed lines. . . . .	56
4.14	Posterior predictive check using the draws of the detector coefficients $a$ and $b$ for the kinematic bin $1250 \text{ MeV} \leq E_\gamma < 1310 \text{ MeV}, 0 \leq \cos \theta < 0.17$ . Points with error bars are the polarization weighted sum of event yields. The dashed line is the mean of the predictive values while the solid opaque lines are representative of one simulation draw $a^{(s)}, b^{(s)}$ . . . . .	57
4.15	Final results for the beam asymmetry $\Sigma$ in $\eta$ photoproduction off the proton for all kinematic bins obtained with BAYESIAN methods. They are compared with the results of a least squares fit and an unbinned fit as given in reference [Afz19]. All results agree within statistical error bars or within the widths of marginal posterior distributions. . . . .	59
4.16	Normalized residuals (left) and unaltered distribution (right) of all 10000 fits for the beam asymmetry $\Sigma = (1 - \delta) \cdot \Sigma_1 + \delta \cdot \Sigma_2$ . GAUSSIAN fits are performed with results given on top of each plot. . . . .	61
4.17	Normalized residuals (left) and unaltered distribution (right) of all 10000 fits for the background beam asymmetry $\Sigma_t^{\text{bkg}}$ . GAUSSIAN fits are performed with results given on top of each plot. . . . .	62
4.18	Fitted efficiency function (red line) applied to the polarization weighted sum of event yields (data points) for one toy Monte Carlo bin. 12 bins in $\phi$ are built for demonstration. . . . .	62
4.19	Combined (added) posteriors of all 1000 fits. Left: Signal beam asymmetry $\Sigma_1$ Right: Background beam asymmetry $\Sigma_t^{\text{bkg}}$ . A GAUSSIAN fit is performed with results given on top. . . . .	63
4.20	Combined (added) posteriors of all fits for the fit parameter $\Sigma_2^{\text{true}}$ . A GAUSSIAN fit is performed which reproduces exactly the values that were used for the simulations. . . . .	64
4.21	MCMC diagnostics for the event based BAYESIAN fit. Left: MCSE, Right: $\widehat{R}$ -value. The critical values not to be exceeded are marked by the dashed lines. . . . .	65
4.22	Posterior predictive checks of one toy Monte Carlo bin using the draws from the marginal posteriors of the detector coefficients $a, b$ (opaque blue lines). The mean values are marked by the dashed line and follow the distribution of the data points which are the polarization weighted sum of event yields, using 12 $\phi$ bins. . . . .	65
4.23	Final results for the beam asymmetry $\Sigma$ in $\eta'$ photoproduction. Two sets of results are shown: The dark blue distributions and orange data points with errorbars are obtained with an unbinned fit that does not consider any background contributions. The light blue distributions and data points are obtained with the modified BAYESIAN fit and by correcting the point estimates according to Equation (4.42), respectively. All errors are statistical errors only. . . . .	67
4.24	Results for the additionally fitted $\Sigma_2^{\text{true}}$ (distributions) compared with the underlying data points [mahlbergphd] with statistical errors. The error bars on average cover $1\sigma$ of the distributions, indicating a successful fit. All errors are statistical errors only. . . . .	68

4.25	MCMC diagnostics for the event based BAYESIAN fit. Left: MCSE, Right: $\hat{R}$ -value. The critical values not to be exceeded are marked by the dashed lines. . . . .	69
4.26	Posterior predictive checks of the kinematic bin $1700 \text{ MeV} \leq E_\gamma < 1800 \text{ MeV}$ , $0.67 \leq \cos \theta < 1$ using the draws from the marginal posteriors of the detector coefficients $a, b$ (opaque blue lines). The mean values are marked by the dashed line and follow the distribution of the data points which are the polarization weighted sum of event yields, using 12 $\phi$ bins. . . . .	69
4.27	Final results for the beam asymmetry $\Sigma_{\eta'}$ for all energy and angular bins. Only the corrected results from the unbinned maximum likelihood fit and distributions from the modified BAYESIAN fit are shown. The bottom of each plot indicates the systematic error as gray bars. It was determined as previously discussed. . . . .	71
5.1	Results for the beam asymmetry $\Sigma_{\eta'}$ (orange errorbars and distributions) compared with the results for the energy bins $E_\gamma = 1569 \text{ MeV}$ , $E_\gamma = 1676 \text{ MeV}$ , $E_\gamma = 1729 \text{ MeV}$ reported in reference [collins] (black errorbars). Systematical errors are shown as grey bars. . . . .	74
5.2	Results for the beam asymmetry $\Sigma_{\eta'}$ (orange errorbars and distributions) compared with PWA solutions: etaMAID [etaMAID](dashed black line),. . . The errorbars only depict statistical error, the systematic error is shown as grey bars. . . . .	76
A.1	Coplanarity $\Delta\phi$ for all energy and angular bins. Data points are displayed as open circles, scaled Monte Carlo data belonging to $\eta'$ photoproduction is displayed as solid histogram. The determined cut ranges are indicated by the dashed red lines. . . . .	83
A.1	Coplanarity $\Delta\phi$ for all energy and angular bins. Data points are displayed as open circles, scaled Monte Carlo data belonging to $\eta'$ photoproduction is displayed as solid histogram. The determined cut ranges are indicated by the dashed red lines. . . . .	84
A.2	Polar angle difference $\Delta\theta$ for all energy and angular bins. Data points are displayed as open circles, scaled Monte Carlo data belonging to $\eta'$ photoproduction is displayed as solid histogram. The determined cut ranges are indicated by the dashed red lines. . . . .	85
A.2	Polar angle difference $\Delta\theta$ for all energy and angular bins. Data points are displayed as open circles, scaled Monte Carlo data belonging to $\eta'$ photoproduction is displayed as solid histogram. The determined cut ranges are indicated by the dashed red lines. . . . .	86
A.3	Missing mass $m_x$ for all energy and angular bins. Data points are displayed as open circles, scaled Monte Carlo data belonging to $\eta'$ (black), $2\pi^0$ (yellow) and $\pi^0\eta$ (magenta) photoproduction is displayed as solid histogram while their sum is displayed as turquoise histogram. The determined cut ranges are indicated by the dashed red lines. . . . .	87
A.3	Missing mass $m_X$ for all energy and angular bins. Data points are displayed as open circles, scaled Monte Carlo data belonging to $\eta'$ (black), $2\pi^0$ (yellow) and $\pi^0\eta$ (magenta) photoproduction is displayed as solid histogram while their sum is displayed as turquoise histogram. The determined cut ranges are indicated by the dashed red lines. . . . .	88
A.4	Invariant mass $m_{\text{meson}}$ for all energy and angular bins. Data points are displayed as open circles, scaled Monte Carlo data belonging to $\eta'$ (black), $2\pi^0$ (yellow), $\pi^0\eta$ (magenta), $\pi^0$ (green) and $\omega$ (blue) photoproduction is displayed as solid histogram while their sum is displayed as turquoise histogram. The determined cut ranges are indicated by the dashed red lines. . . . .	89

- A.4 Invariant mass  $m_{\text{meson}}$  for all energy and angular bins. Data points are displayed as open circles, scaled Monte Carlo data belonging to  $\eta'$  (black),  $2\pi^0$  (yellow),  $\pi^0\eta$  (magenta),  $\pi^0$  (green) and  $\omega$  (blue) photoproduction is displayed as solid histogram while their sum is displayed as turquoise histogram. The determined cut ranges are indicated by the dashed red lines. . . . . 90
- B.1 Fit performance in dependence of the number of bins. Left axis shows the mean  $\mu$  of the distribution of the normalized residuals  $\xi$ , right axis shows the mean  $\chi^2$  of all fits. Squares simulate fits with statistics similar to the  $\gamma p \rightarrow p\eta' \rightarrow p\gamma\gamma$  final state, triangles statistics similar to the  $\gamma p \rightarrow p\eta \rightarrow p\gamma\gamma$  and final state, pentagons statistics similar to the  $\gamma p \rightarrow p\pi^0 \rightarrow p\gamma\gamma$ . Dotted red line indicates the ideal value of  $\chi^2 = 1$ , while the dashed blue line indicates the ideal mean of the normalized residuals at  $\mu = 0$ . 92
- C.1 Combined posteriors of all 1000 fits without truncation for the signal beam asymmetry  $\Sigma_1$  and the background beam asymmetry  $\Sigma_t$ . Left: normalized residuals  $\Xi$ , Right: unaltered added posterior distributions. GAUSSIAN fits have been performed with results given on top of each plot. . . . . 94
- C.2 Posterior distributions of  $\Sigma_1$  (left) and  $\Sigma_t$  (right) combined in an independent likelihood pool. GAUSSIAN fits to the distribution confirm the reproduction of the input values within  $1\sigma$ . Note that only very few datapoints were available for the fits, because the distributions overwhelmingly converge into a single bin at  $\pm 0.5$ , hence the large errors on the fit parameters. . . . . 95

# List of Tables

---

1.1	Summary of the particles of the SM . . . . .	1
1.2	Allowed quantum numbers for the intermediate resonance state $N^*/\Delta^*$ . . . . .	4
3.1	The five most probable decay modes of the $\eta$ and $\eta'$ meson. The most probable further decay with according branching ratio is shown in brackets.[ <b>pdg</b> ] . . . . .	11
3.2	Examined MC reactions that were used in sum for the fit . . . . .	17
3.3	Fit functions and cut ranges for each kinematic variable . . . . .	18
3.4	Total cross sections $\sigma$ in the energy range 1500 to 1800 MeV, branching ratios (BR) to $n\gamma$ final states, maximum acceptance $\tilde{A}$ for signal and possible background contributions as well as the expected signal to background ratio $R$ . References [ <b>2pi0`cs</b> ] and [ <b>pi0eta`cs</b> ] give the cross sections only up to roughly 1500 MeV, the given values are thus upper bounds. For the same reason, from reference [ <b>3pi0cs</b> ] only a lower bound can be estimated. For all other reactions a rough mean over the energy bins of interest is built. If the references provide only differential cross sections a crude integration in each angular bin is performed. In case only very few ( $O(10^1)$ ) decays pass event selection, the acceptance is built in one global bin only for the respective reactions. This is indicated by the horizontal line. . . . .	26
3.5	Relative loss in signal and background events if a cut on $\Delta E$ is applied. . . . .	32
4.1	Summary of the complete setting of all toy Monte Carlo experiments for the event based fit. Values and table layout adapted from [Afz19]. . . . .	49
4.2	Summary of the complete setting of all toy Monte Carlo experiments for the event based fit. Table layout adapted from [Afz19]. . . . .	60